



Atom probe tomography study of alloying element distributions in Zr alloys and their oxides



Yan Dong^a, Arthur T. Motta^b, Emmanuelle A. Marquis^{a,*}

^aDepartment of Materials Science and Engineering, University of Michigan, Ann Arbor, MI 48109, United States

^bDepartment of Mechanical and Nuclear Engineering, Penn State University, University Park, PA 16802, United States

ARTICLE INFO

Article history:

Received 10 June 2013

Accepted 31 August 2013

Available online 8 September 2013

ABSTRACT

A detailed study of alloying element distributions in the metal and oxygen rich regions of corroded Zr alloys and of the phases formed ahead of the oxide front was conducted using atom probe tomography (APT). A consistent sequence of sub-oxide phases is observed ahead of the ZrO₂ oxide front, consisting of (i) a thin layer of equiatomic ZrO (occasionally slightly over and under stoichiometric) (ii) saturated solid solution Zr(O)_{sat}, and (iii) a slowly decreasing oxygen profile into the metal. The results also show that the distribution of the alloying elements in the metal is more inhomogeneous than previously thought and that in the oxygen-rich phases enhanced segregation is observed, compared to the metal.

© 2013 Elsevier B.V. All rights reserved.

1. Introduction

Zirconium based alloys are widely used as nuclear fuel cladding materials in nuclear power plants because of their low thermal neutron capture cross-section, adequate mechanical behavior and good high temperature corrosion resistance [1]. Yet waterside corrosion and its associated hydrogen pickup remain a major issue for utilizing these alloys in severe fuel duty conditions, especially in pressurized water reactors [2]. Alloys with greater corrosion resistance are required to ensure continued fuel efficiency and reliability as burnup increases.

The key to improvements realized in corrosion resistance over the last decades has been a continuous improvement in alloy performance, brought about by incremental alloy modifications and by the introduction of new alloys such as M5 and ZIRLO, which exhibit much better corrosion performance than Zircaloy-4 in the same corrosion environment [3,4]. The difference between the corrosion performance of different alloys is sought in the differences in the structure of the protective oxides formed on these alloys [2]. Much work has been performed in this area, using various techniques, such as cross sectional transmission electron microscopy (TEM), Raman spectroscopy, microbeam synchrotron radiation diffraction and fluorescence to characterize the structure of the layer, including crystal structure, texture, grain size and morphology, porosity and cracking [5–14]. Various authors have reported on the various oxide phases formed including the specific mixture of monoclinic and tetragonal ZrO₂ observed, columnar grain morphology, etc. [15–20].

The determination of the alloying element distribution and precursor oxide phases has received comparatively less attention. The alloying elemental distributions because of their low concentration and fine spatial resolution are most precisely studied with atom probe techniques. Wadman et al. [21] studied the base Zircaloy-2 using 1D atom probe, but did not benefit from very good statistics. More recently Thuvander et al. [22] reassessed the analysis of minor elements in the same alloy. Hudson et al. [23] performed analysis on oxidized Zircaloy-4, Zr–Nb and ZIRLO using pulsed laser field evaporation. More recently, using the same technique, Sundell et al. [24] and Teijland et al. [25] analyzed in detail solute concentrations in oxidized Zircaloy-2, while Wei et al. [26] analyzed the distribution of Sn in corroded Zr–Nb–Sn alloys with different Sn contents.

Several lower stoichiometry metastable oxide phases are predicted from the phase diagram and have been reported by individual researchers using TEM or microbeam synchrotron radiation diffraction [15,20,27–29]. In particular, detailed studies of the oxide–metal interface found by atom probe tomography (APT) that the lower stoichiometry metastable oxide phase, which according to their measurements is ZrO, was present only at pre-transition stage, disappeared after post-transition [19,20]. More recently, Hutchinson et al. [18] observed a region of varying oxide stoichiometry that extends for more than a hundred nanometers into the oxide beneath the metal–oxide interface. They considered this layer as a barrier layer where transport of oxygen takes place by ionic diffusion with important implications for the oxidation process. A summary of some of these results was presented by Preuss et al. [30].

These precursor layers could affect the corrosion kinetics in two principal ways: by using up oxygen that could have been used to form ZrO₂ they slow down the oxide layer advance and by

* Corresponding author. Tel.: +1 7347648717.

E-mail address: emarq@umich.edu (E.A. Marquis).

presenting a different material ahead of the advancing oxide they can affect the oxide corrosion kinetics and, possibly the onset of the oxide transition. For example, it has been proposed that the hardening of the matrix near the oxide makes it difficult for the metal to plastically deform to relieve oxide growth stresses. The presence of these layers has also been shown to correlate with the kinetics of oxidation [16], such that the width of the suboxide layer inversely correlates with the corrosion kinetics. Similar results were seen in the examination of oxides formed in supercritical water corrosion at 500 °C [27]. In that instance much thicker suboxide layers were formed that actually had to be accounted for in order to rationalize the weight gain.

Fig. 1 shows the corrosion weight gain of various Zr alloys as a function of exposure time in 360 °C pure water during an autoclave test. Zircaloy-4 (black diamonds) shows the well-known saturating growth behavior with well-defined periodic transitions. Pure Zr and alloys such as Zr–0.5Cr lose protectiveness right away, while others such as Zr–1.0Cu show gradually increased corrosion rate. One of the alloys studied (Zr–0.4Fe–0.2Cr) showed protective behavior for the whole duration of the test (500 days). It is notable that the alloying content variation between these alloys is very small, and yet their behaviors run the gamut from totally protective to immediately non-protective. From these results it is clear that the alloying elements play a role, as yet to be determined, in the protective character of the oxide layer.

To discern this role it is clear that the alloying element distribution in both the alloy and in the oxide layer could be important. For the metal alloy distribution the majority of alloying elements is in precipitates but a fraction could also be dissolved in the matrix, associated with other alloying elements and microstructure features [31]. Concerning the oxide, questions remain as to which elements might be rejected ahead of the oxide front, and whether segregation occurs to the oxide grain boundaries. Such small elemental variations are best studied by atom probe tomography.

In present study, the microstructure and chemistry of the three regions of greatest interest- the oxide, the oxide–metal interface and the metal bulk- were studied using APT. The characterization was performed on three zirconium alloys with different alloying additions in order to investigate the correlation between the distribution of alloying elements and the development of the oxide layers.

2. Experimental methods

The alloys studied were pure Zr (crystal bar), Zircaloy-4, and Zr–0.4Fe–0.2Cr. The nominal chemical compositions of the alloys

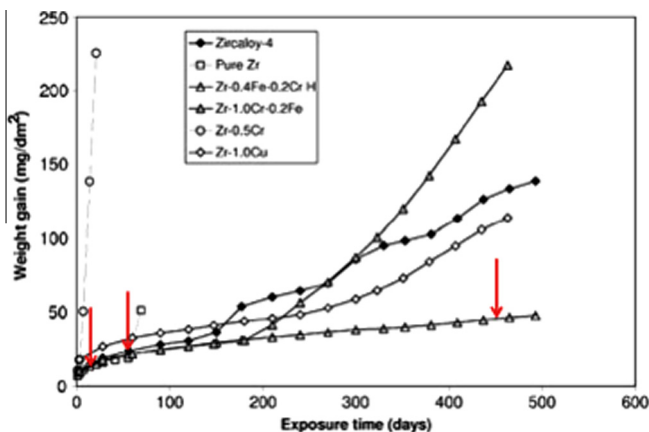


Fig. 1. Corrosion weight gain-exposure time for studied alloys oxidized in 360 °C water [14].

were measured by vacuum hot extraction and are given in Table 1. The measurements by APT are comparable to those by HVE, at least for the elements homogeneously distributed over the matrix (which is not the case for Fe and Cr as mentioned below).

Coupons of these alloys were autoclave corroded in 360 °C water following ASTM Practice (G2-88) as part of a previous research project [14,27]. The corrosion behavior was evaluated by measuring the weight gain versus exposure time curve, as shown in Fig. 1. The alloy samples used in this study are listed in Table 2. All of the three samples examined in this study were in the protective regime.

Cross-sectional samples were cut from the oxidized coupons and ground on 1200 grit SiC paper on both cross sectional sides. One side of the sample was polished using successively finer polishing cloth to 0.5 μm diamond. The needle-shaped samples for atom probe tomography were prepared using a focused ion beam (FIB)-based lift-out method, which allowed selective extraction of volumes containing metal/oxide interfaces. APT samples with different orientations of interfaces (either parallel or perpendicular to the needle axis) were fabricated to better investigate both the interface region and the oxygen ingress into metal (Fig. 2). Pt was deposited as protective layer and the standard lift-out procedure was applied [32]. A final 2 kV clean-up procedure was utilized to remove any remaining Pt and to minimize Ga damage.

The lift-out samples were analyzed using a CAMECA LEAP-4000XHR operated in a laser pulsing mode with 200 kHz pulse repetition rate and 70–100 pJ laser energy. The temperature of the specimens was maintained at 50 K while the standing voltage was varied automatically to maintain a detection rate of 0.005 ion/pulse. The collected data was reconstructed and analyzed using the reconstruction software, IVAS 3.6.6. The default value of the image compression factor (3.3) and the evaporation field of Zr (28 V/nm [33]) were selected for reconstruction. The composition measurement was done separately for each phase and a peak decomposition technique was used to deconvolute the Zr^{3+} peak from the O_2^+ peaks, which overlap at 32 mass-to-charge ratio.

3. Results

A total of more than 34 needles were studied from the different regions of the three alloy samples, both in the metal and in the oxide. Most APT datasets contain more than 20 million ions to ensure a good statistics. In this section we report the experimental results obtained on the three alloys examined, from needles fabricated at different locations in the bulk and in or near the oxide layers.

3.1. Solute distribution in bulk alloy (away from oxide scale)

3.1.1. Crystal bar

APT samples taken in the bulk of the alloy, i.e. far away from the oxidized surface ($\sim 200 \mu\text{m}$), show a generally uniform distribution of Cr without any evidence of clusters or indication of elemental segregation to microstructure features such as grain boundaries or dislocations. No Fe was detected in this volume – note that the detection limit for Fe was about 0.002 at.% (12 wt ppm). Concentration measurements from the APT datasets matched the Zr and Cr concentrations measured using hot vacuum extraction as shown in Table 1. Small amounts of C, O and Al were also detected. The low Fe concentration measured in the matrix is reasonable. The alloy is in a recrystallized state with a final heat-treatment temperature corresponding to an extremely low solubility of Fe in Zr [34]. The reported maximum solubility of Fe in α -Zr is 120 wt ppm (0.02 at.%) at 800 °C and less than 50 wt ppm at temperatures lower than 300 °C [35]. Fe is found to be segregated at

Table 1
Chemical composition of zirconium alloy ingots as measured by hot vacuum extraction and matrix composition as measured by APT. Errors of APT measurements are calculated from dataset to dataset variations and counting statistics within each dataset.

Alloys		Sn	Fe	Cr	O	C
Crystal bar Zr	HVE (wt.%)	<0.002	0.009	<0.0005	<0.025 ^a	0.014
	HVE (at.%)	<0.002	0.015	<0.002	<0.14	0.11
	APT (at.%)	N.A.	0.002 ± 0.001	0.002 ± 0.001	0.032 ± 0.002	0.008 ± 0.001
Zircaloy-4	HVE (wt.%)	1.32	0.19	0.094	0.131	0.015
	HVE (at.%)	1.01	0.31	0.16	0.74	0.11
	APT (at.%)	0.99 ± 0.03	0.003 ± 0.002	0.015 ± 0.010	0.9 ± 0.03	0.07 ± 0.04
Zr-0.4Fe-0.2Cr	HVE (wt.%)	<0.002	0.38	0.22	0.112	0.021
	HVE (at.%)	<0.002	0.61	0.36	0.63	0.16
	APT (at.%)	N.A.	0.004 ± 0.002	0.015 ± 0.002	0.68 ± 0.002	0.04 ± 0.002

^a Oxygen value below lowest verifiable calibration point.

Table 2
Corrosion tests conditions of studied alloy samples.

Studied alloy	Exposure time (days)	Weight gain (mg/dm ²)	Estimated oxide thickness (μm)
Crystal bar Zr	7	10.5	0.71
Zircaloy-4	60	27.6	1.88
Zr-0.4Fe-0.2Cr	456	45.6	3.10

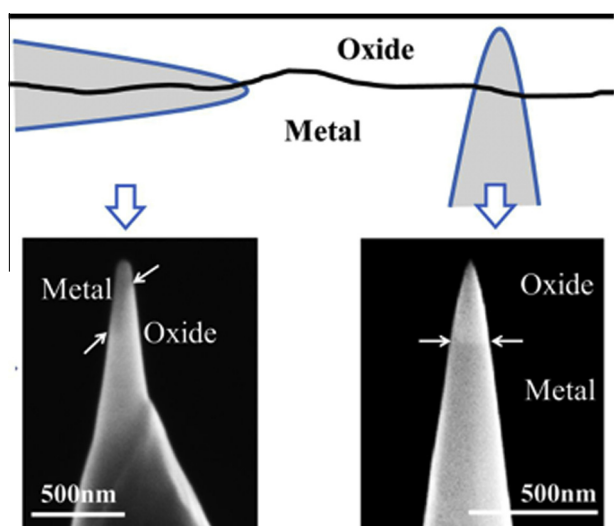


Fig. 2. Schematic illustration and SEM images of the two orientations chosen for the APT specimens.

grain boundaries, as illustrated in Fig. 3. Segregation of other elements is not observed. It is expected that if APT were to be performed over a representative volume of the microstructure containing regions of high iron concentration the values would match.

3.1.2. Zircaloy-4

Zircaloy-4 contains Sn, Fe and Cr as major alloying elements. Sn is found in solid solution and Fe and Cr mostly in intermetallic precipitates of the type $Zr(Cr,Fe)_2$ [35,36]. The matrix Sn concentration was measured from the bulk of the metal far away from the oxide, and calculated from a dataset without grain boundaries and clusters (Table 1). The Fe and Cr matrix concentrations determined by APT were close to the reported solubility limits (0.04 at.% for Cr and 0.02 at.% for Fe at 800 °C [35]), which are much lower than the bulk alloy concentration, since essentially all Fe and Cr are in precipitates.

From previous work [31], the precipitate number density in recrystallized Zircaloy-4 is around $0.7 \times 10^{12} \text{ cm}^{-3}$, and the

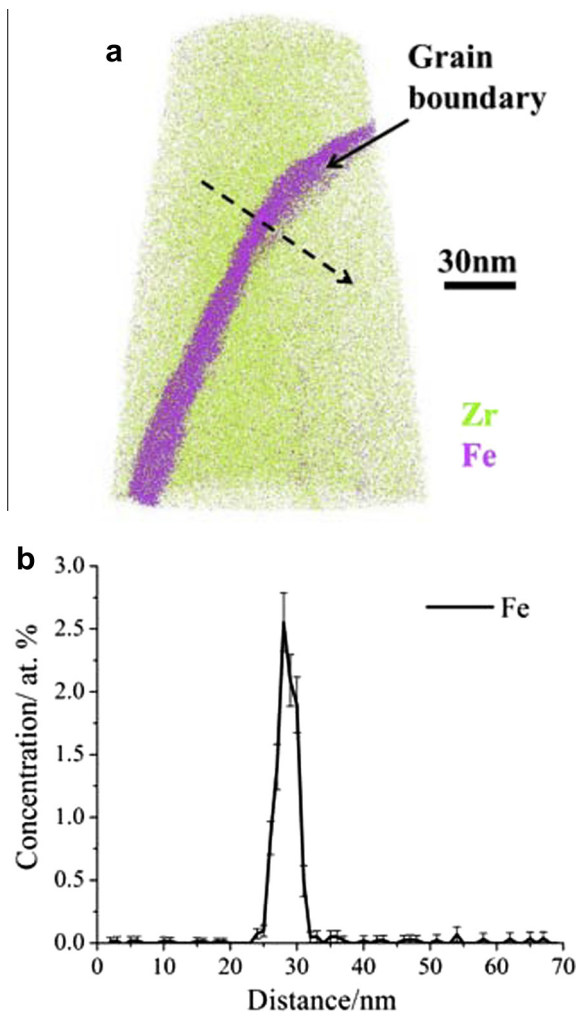


Fig. 3. Bulk crystal bar Zr: (a) APT reconstruction showing a grain boundary with Fe segregation; (b) line profile across grain boundary along the arrow shown in (a).

average spacing between precipitates (usually 0.1–0.3 μm in size) is greater than 1 μm, so it is normal that their capture in the APT specimens is unlikely. However, some small clusters (~5 nm diameter), which would normally be invisible in TEM are occasionally seen by APT, as shown in Fig. 4(a). The apparent composition of these clusters obtained from a proxigram analysis is 89.3% ± 1.9% Zr, 4.8% ± 1.3% Fe, 5.9% ± 0.7%Cr. Note that the measured composition is affected by ion trajectory aberrations from the difference in

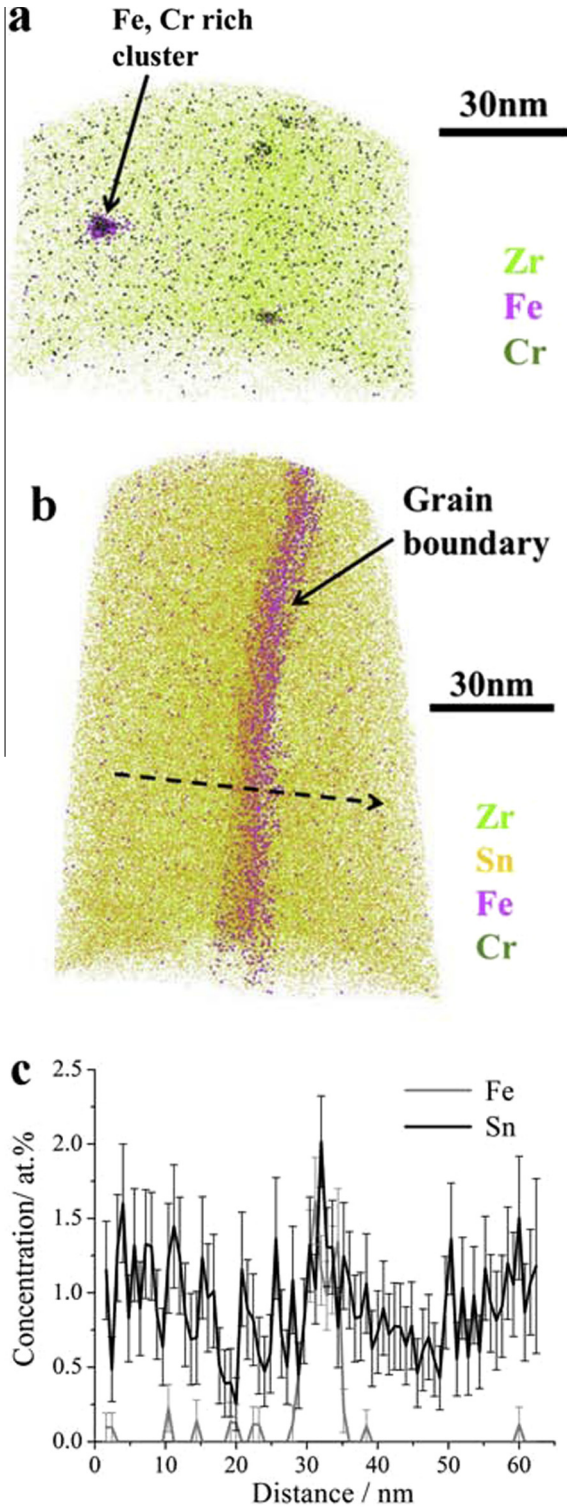


Fig. 4. Bulk Zircaloy-4: (a) APT reconstruction showing Fe, Cr rich clusters; (b) APT reconstruction showing grain boundary with Fe and Sn segregation; (c) line profile across grain boundary along the arrow shown in (b).

evaporation fields between matrix and clusters, as evidenced by the apparent higher density of ions observed at the position of the clusters [37].

Fe and Sn segregation was observed at grain boundaries (Fig. 4(b)). A line profile of concentration through the grain boundary in Fig. 4(c) shows noticeable segregation of Fe (up to 1.5% or a enrichment factor of 5 relative to the alloy bulk and much higher relative to the Fe content in the matrix (Fig. 4(c)). A much less marked segregation of Sn can also be discerned in the same figure. No segregation of other elements was observed on the grain boundary. No evidence was seen for solute segregation to dislocations but this may be because of the low dislocation density in the recrystallized material.

3.1.3. Zr–Fe–Cr

As shown in Table 1, the measured matrix concentrations of Cr and Fe in the bulk of the alloy are much lower than the overall alloy composition, likely because most of the Fe and Cr are usually found in C14 Zr(Cr,Fe)₂ Laves phase precipitates [11,36]. A portion of one such precipitate was caught in one of the needles, as seen in Fig. 5. The measured atomic composition of 34.50% ± 0.11% Zr–43.68% ± 0.10Fe–21.82% ± 0.08%Cr, is in reasonable agreement with the overall stoichiometry of the Zr(Cr,Fe)₂ Laves phase.

Similarly to Zircaloy-4, Fe segregation to grain boundaries is observed to a similar level as in Zircaloy-4 as shown in Fig. 6 and some Al, O and C are also observed in the matrix.

3.2. Oxide scale morphologies and oxide phases

APT specimens were prepared from the oxide and oxide–metal interface regions in the three alloy samples. A series of oxygen-

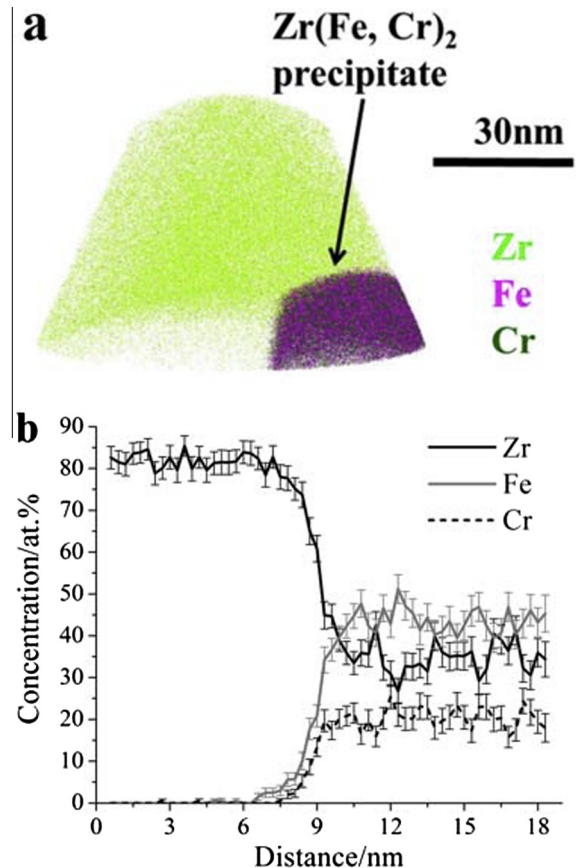


Fig. 5. Bulk Zr–Fe–Cr: (a) APT reconstruction showing part of an Fe, Cr rich intermetallic precipitate; (b) line profile across the precipitate interface.

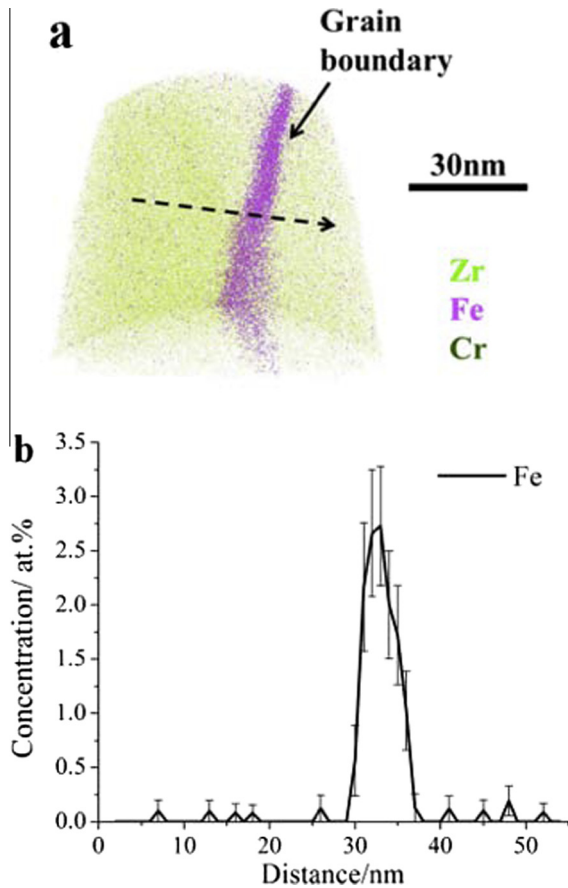


Fig. 6. Bulk Zr–Fe–Cr: (a) APT reconstruction showing the grain boundary with Fe segregation; (b) concentration profile across the grain boundary along the arrow shown in (a).

containing phases are observed for all three alloys. These phases are in order:

- (i) the stable oxide ZrO_2 (which is in contact with water),
- (ii) the equiatomic suboxide ZrO (both slightly sub and superstoichiometric, denoted here ZrO_{1+x} and ZrO_{1-x}),
- (iii) a saturated solution of constant oxygen content at about 30% O, denoted $\text{Zr(O)}_{\text{sat}}$, and
- (iv) an undersaturated solid solution of O in Zr, denoted Zr(O) , the oxygen content of which decreases with distance from the oxide–metal interface.

As stated above, the field evaporation behavior of these phases is drastically different, resulting in characteristic ions being evaporated from each phase. As a result, the phases can be identified both by atomic concentrations and by the nature of the ionic species evaporating from each phase. The latter method was also used to visualize the distribution of phases within needles. For example, it was found in the present study that oxygen was evaporated as O^+ , O_2^+ , ZrO^{2+} , ZrO^{3+} , ZrO_2^+ , ZrO_2^{2+} , ZrO_3^+ with occasional instances of $\text{Zr}_2\text{O}_3^{3+}$ and $\text{Zr}_2\text{O}_3^{3+}$ observed. Zr ions (Zr^{2+} , Zr^{3+}) become significant in the $\text{Zr(O)}_{\text{sat}}$ phase. O_2^+ is only observed in the oxide (ZrO_2) phase, so it is considered a marker for that phase. ZrO_2^+ and ZrO_2^{2+} are present both in the ZrO_2 and ZrO_{1+x} phases but absent in the ZrO_{1-x} , $\text{Zr(O)}_{\text{sat}}$ and Zr(O) phase.

3.2.1. Crystal bar Zr

A representative APT dataset from a needle prepared containing the oxide–metal interface of crystal bar Zr is shown in Fig. 7. A minor fracture occurred as the tip was being evaporated; the data

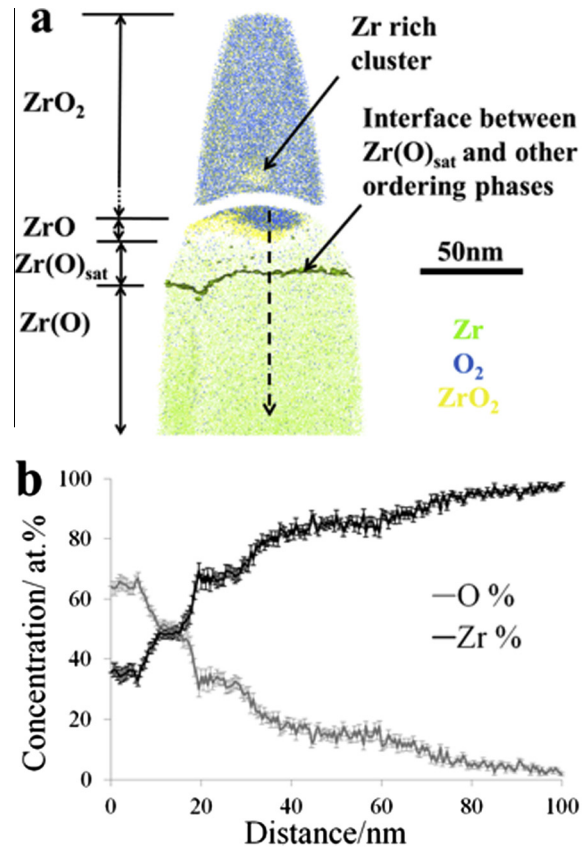


Fig. 7. Crystal bar Zr oxide region: (a) a 10 nm slice from an APT reconstruction containing the oxide/metal interface; (b) concentration profile along the arrow indicated shown in (a).

collected before and after the fracture were reconstructed separately and shown in Fig. 7(a). A Zr iso-surface is used to indicate the interface between $\text{Zr(O)}_{\text{sat}}$ and the solid solution as shown in Fig. 7(a). The same iso-surface is used in other figures whenever relevant with the same purpose. The line profile in Fig. 7(b) was obtained by integrating the contents of a cylinder perpendicular to the interface, as indicated by the arrow in Fig. 7(a). The resulting oxygen concentration profile taken along the reconstruction axis, shows that the composition of the top oxide layer is consistent with that of ZrO_2 . The sequence of phases follows the above: an intermediate layer is observed beneath the ZrO_2 layer with a composition corresponding to ZrO (a ZrO cluster is also observed near the ZrO_2/ZrO interface but inside the ZrO_2 phase). In the metal region adjacent to ZrO , the saturated solid solution layer with 31–32% oxygen content, $\text{Zr(O)}_{\text{sat}}$ is observed. The region of undersaturated solid solution follows with a continuously decreasing oxygen profile into the metal. The phase diagram shows many ordered phases of Zr(O) solid solution, and it is possible that some of these are present at the distance 30 nm (corresponding to Zr_3O) to 50 nm (approx. Zr_4O) considering the slope changes at that location, but their presence remain to be confirmed. The intermediate oxide layers ($\text{ZrO}/\text{Zr(O)}_{\text{sat}}$) in crystal bar Zr are quite thin (less than 20 nm).

3.2.2. Zircaloy-4

The examination of a needle taken from the oxide–metal interface of Zircaloy-4 shows a similar oxide sequence as that seen in crystal bar Zr, but with thicker intermediate layers of ZrO and $\text{Zr(O)}_{\text{sat}}$. One dataset with interface perpendicular to the tip axis (vertical) and two reconstructed datasets with the interface

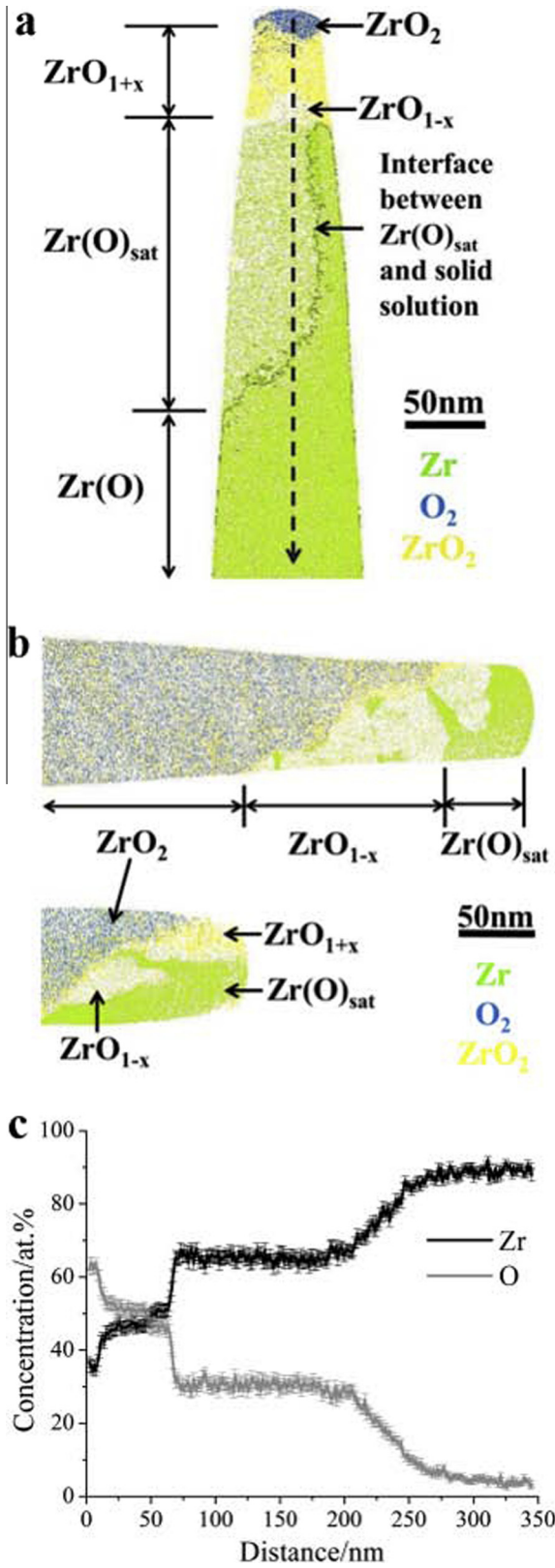


Fig. 8. Zircaloy-4 oxide region: (a) 10 nm slice from an APT reconstruction showing the presence of different oxide phases; (b) 10 nm slices from two distinct APT reconstructions showing the morphologies of the various interfaces; (c) concentration profile taken along the arrow indicated in (a).

oriented parallel to the tip axis (horizontal) are given in Fig. 8(a) and (b). The line profile across the arrow in Fig. 8(a) is shown in Fig. 8(c). The ZrO layer is about 50–100 nm thick, and the Zr(O)_{sat}

about 100–150 nm thick. More detailed examination shows that the ZrO layer actually consists of two layers with slightly different compositions, slightly above and slightly below stoichiometry. As seen in Fig. 8(a), in this sample also the region represented by ZrO_{1+x} (in yellow) has a composition slightly rich in O while the region denoted ZrO_{1-x} (in white) is slightly deficient in O. The interface between the ZrO₂ oxide and suboxide ZrO is relatively smooth, while the interface between suboxide and matrix is rougher, see for example, the Zr(O)_{sat}/Zr interface in Fig. 8(a) and the ZrO_{1+x}/Zr interface in Fig. 8(b).

3.2.3. Zr–Fe–Cr

The same sequence of suboxide and oxide phases seen in crystal bar Zr and Zircaloy-4 is observed in the Zr–Fe–Cr alloy. However, the intermediate ZrO layer is much thicker (at least 300 nm) than seen in crystal bar Zr and Zircaloy-4. As a result, the needle used for APT analyses fractured before reaching the solid solution region. One of the reconstructed datasets is shown in Fig. 9(a). As above, the interface between ZrO₂ and ZrO is relatively smooth. On the other hand, the morphology of the ZrO/Zr(O)_{sat} transition is complex and quite different from that seen in Zircaloy-4. Both rod-shaped and plate-shaped Zr-rich regions (possibly Zr(O)_{sat}) are seen with the ZrO phase in Fig. 9(a). A concentration profile of this Zr rich region is shown in Fig. 9(b).

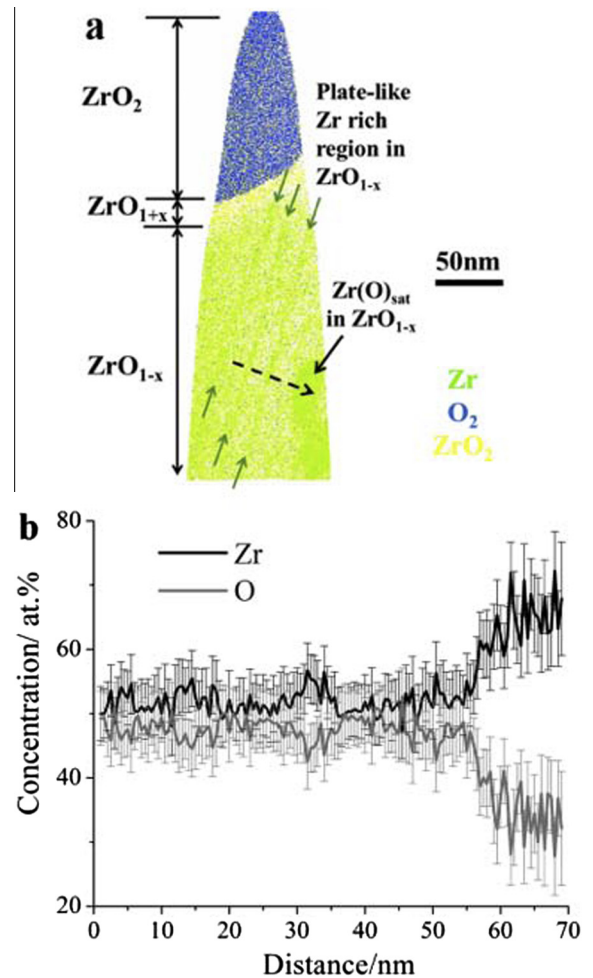


Fig. 9. Zr–Fe–Cr oxide region: (a) 10 nm slice from an APT reconstruction showing the presence of different oxide phases and oxide morphology; (b) concentration profile taken along the arrow indicated in (a).

3.3. Distribution of alloying elements near the oxide metal interfaces

The distribution of other alloying elements in the metal region next to the oxide, (where significant oxygen diffusion has occurred) is different from that in the bulk of the material. This is reasonable since the phase equilibria should be altered by the presence of oxygen. These results are summarized in this section.

3.3.1. Crystal bar Zr

Within the oxide and suboxide regions, Fe is found to segregate to the interface between ZrO_2 and ZrO (Fig. 10(a)) and to grain boundaries in $Zr(O)_{sat}$ and the solid solution region (Fig. 10(b)). The oxygen level is also higher at the grain boundary (Fig. 10(c)), indicating possible preferential grain boundary oxidation in crystal bar Zr.

3.3.2. Zircaloy-4

The distribution of alloying elements in the oxygen rich region of the metal is more complicated in Zircaloy-4 than in crystal bar Zr. Generally, within the stoichiometric ZrO_2 oxide, the Sn concentration is lower than that in the suboxide and in the metal. The Sn/

Zr ratio is also slightly lower in ZrO_2 but the variation of this value among different datasets is relatively large due to high background in the mass spectrum. No Fe or Cr was detected in ZrO_2 oxide matrix (below the detection limit) (Table 3).

In the $Zr(O)_{sat}$ region adjacent to ZrO suboxide, Fe and Cr-rich fine clusters are occasionally observed (Fig. 11(b)), indicating a tendency to Fe rejection from the ZrO suboxide phase. Fe is also found to segregate to linear features, possibly dislocations, formed in the region near the oxide metal interface which has been plastically deformed by the growing oxide (Fig. 11(a) and (b)).

Segregation of Sn is observed between ZrO and the saturated solid solution $Zr(O)_{sat}$. The segregation to the $Zr(O)_{sat}/ZrO$ is strongly dependent on the local curvature of the interface. Higher levels of Sn are observed in the region between the ZrO fingers seen at the interface (Fig. 12(a)). The local concentration of Sn between the ZrO fingers goes up to around 3.5%, which is higher than Sn concentration in the metal bulk (Fig. 12(b) and Fig. 12(c)). Interestingly, Sn also exhibits inhomogeneous distribution within the ZrO_2 oxide layer, to planar type features whose spacing is similar to the measured columnar oxide grain width in these samples, about 30–50 nm (Fig. 12(a)), indicating a possible segregation of Sn to oxide grain boundaries.

Planar-like segregation of Fe and Sn is also observed beneath the ZrO suboxide layer, indicating possible grain boundary segregation of these elements induced by the oxygen. A slice of the dataset containing grain boundaries is shown in Fig. 13(a), along with a concentration profile. The concentration of Fe (segregation factor) is quite high for Fe, since the concentration is ~2.5% (Fig. 13(b)), to be compared with 0.2% in the alloy and 10 s of ppm in the matrix solid solution. In contrast to the observation in crystal bar Zr, no increase of oxygen content is seen at grain boundaries of Zircaloy-4 (Fig. 13(c)).

3.3.3. Zr–Fe–Cr

In Zr–Fe–Cr alloy, Fe segregates to $Zr(O)_{sat}/ZrO$ interfaces, as shown in Fig. 14(a). Fe is also found to form clusters on planar and linear features within ZrO_2 (Fig. 14(b)), possibly as a result of Fe segregation to oxide grain boundaries and/or dislocations. Grain boundaries showing Fe segregation were also observed in $Zr(O)_{sat}$ phase and the Fe segregated to one of the boundaries is still seen segregated in the ZrO phase (Fig. 14(a)). There are not enough datasets that can give information about clustering and other possible segregations beneath the ZrO layer.

4. Discussion

A detailed study characterizing the alloying element distributions using atom probe tomography has been performed for three Zr alloys (crystal bar Zr, Zircaloy-4 and ZrFeCr model alloy), which exhibit a range of corrosion kinetics and behavior. The results of this initial effort have shed some light on the differences between alloys. In general, the current observations regarding the overall concentrations and distribution of alloying elements in the metal, the oxides, and the oxide metal interface are in general agreement with existing knowledge, but provide greater detail on compositions and alloying element distributions.

4.1. Oxide phases

Oxide formation in the three alloys showed some similarities. All oxide layers examined showed precursor phases of various oxygen contents. The sequence of phases observed from the oxide water interface to the metal was the same in all alloys, starting with ZrO_2 (corresponding to the traditional oxide layer, which

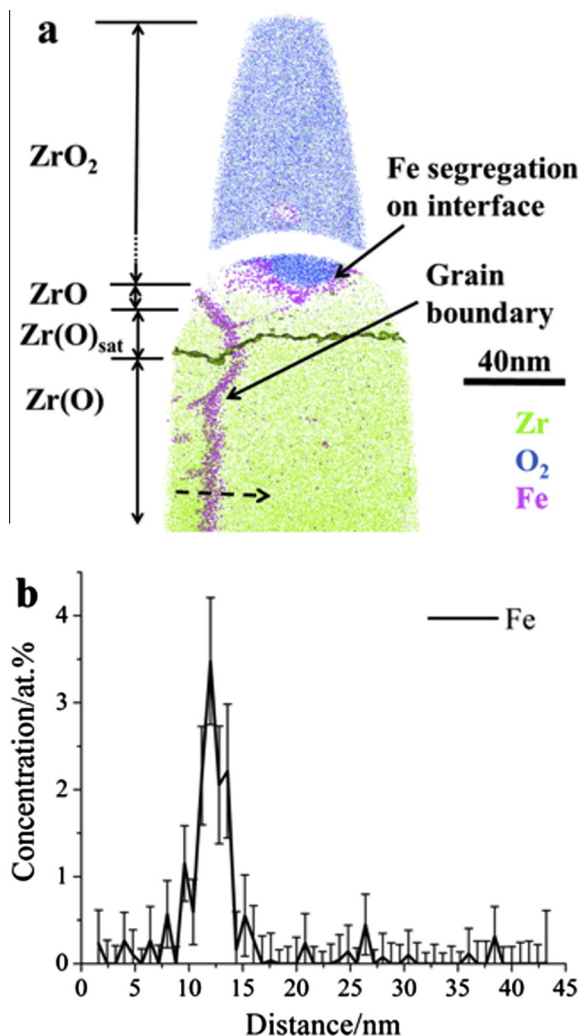


Fig. 10. Crystal bar Zr oxide region: (a) 10 nm slice from an APT reconstruction showing the distribution of Fe at the interface and grain boundary; (b) and (c) concentration profiles of Fe and O across the grain boundary along the arrow indicated in (a).

Table 3

Compositions in each oxide matrix in all three alloys (at.%). Errors are calculated from dataset to dataset variations and counting statistics within each dataset.

Alloy	Oxide phases	Zr	O	Sn	Fe	Cr	Sn/Zr (%)
Crystal bar Zr ^b	ZrO ₂	33.2 ± 1.1	66.80 ± 1.06	N.A.	<0.003	<0.003	N.A.
Zircaloy-4 ^c	ZrO ₂	31.9 ± 3.6	67.8 ± 3.6	0.3 ± 0.05	<0.004	<0.004	0.89 ± 0.13
	ZrO _{1-x}	51.1 ± 0.8	48.1 ± 0.8	0.6 ± 0.02	<0.004	<0.004	1.07 ± 0.03
	Zr(O) _{sat}	68.0 ± 0.9	31.2 ± 1.0	0.8 ± 0.02	0.02 ± 0.002 ^a	0.02 ± 0.005	1.01 ± 0.03
Zr-Fe-Cr ^c	ZrO ₂	33.5 ± 0.8	66.4 ± 0.9	N.A.	<0.01	<0.01	N.A.
	ZrO _{1-x}	51.1 ± 0.7	48.8 ± 0.8	N.A.	<0.01	<0.01	N.A.
	Zr(O) _{sat}	67.6 ± 1.0	32.4 ± 1.0	N.A.	0.02 ± 0.002 ^a	<0.01	N.A.

^a Fe content in Zr(O)_{sat} is overestimated due to high density of dislocations with Fe segregation in Zr(O)_{sat} in Zircaloy-4 and presence of grain boundaries in Zr-Fe-Cr.^b Composition of intermediate suboxide in crystal bar Zr is not available because the volume is too small for composition measurement.^c Composition of ZrO_{1-x} phase in Zircaloy-4 and Zr-Fe-Cr is not available because the volume of the phases is too small for composition measurement.

went from the oxide water interface to the oxide metal interface), followed by a sequence of suboxide phases in order, as summarized in Fig. 15:

- (i) the equiatomic ZrO phase (observed as both ZrO_{1+x} and ZrO_{1-x}),
- (ii) a plateau of the saturated solid solution Zr(O)_{sat},
- (iii) a slowly decreasing oxygen profile, with some hints of specific phases.

The present results are in broad agreement with the literature. Using atom probe tomography and electron energy loss spectrometry (EELS), Hutchinson et al. [18], Ni et al. [19,20], Hudson [23], and Preuss et al. [30] reported the presence of a ZrO equiatomic layer on corroded Zirco, Zircaloy-2 and Zircaloy-4. Electron diffraction analysis found a fcc structure for ZrO [19]. The ZrO layer was not detected in a previous study using microbeam synchrotron radiation diffraction study [14], likely due to insufficient spatial resolution. The presence of the Zr(O)_{sat} layer has also been observed by Ni et al. [19] and previous examinations by TEM and synchrotron radiation showed a 30% oxygen layer (Zr₃O) ahead of the oxide scale, with different thicknesses in Zircaloy-4, Zr₂5Nb and ZIRLO [14,15]. The presence of an ω-Zr phase with 40 at.% O [17] ahead of the oxide front was also reported.

The Zr–O phase diagram at the temperatures and compositions of interest would predict the observation of an equilibrium between a supersaturated solution of oxygen in hcp α-Zr (about 30 at.% O) with monoclinic ZrO₂ [38]. Additional metastable ordered phases in Zr are predicted for lower oxygen content and lower temperatures [38], representing various arrangements of oxygen in the interstitial sites of the hcp structure. Recent thermodynamic studies show several other phases [39] also found stable low oxygen ordered phases (Zr₆O and Zr₃O) – which the authors suggest are highly hypothetical – for temperatures below 300 and 350 °C. They also predicted the existence of a line compound Zr₂O ordered phase stable to higher temperatures, which does not appear in the phase diagram [38]. Recent first-principle calculations have identified a stable ZrO phase with an hexagonal ω-Zr structure with O interstitials and determined that a phase with a Zr₂O stoichiometry (and thus close to the Zr(O)_{sat} phase predicted by the phase diagram as the solubility limit of O in Zr) forms by oxygen ordering within the hcp Zr sublattice with a range of oxygen concentration [40].

The present observations with the sequence of Zr(O)_{sat}, ZrO, ZrO₂, could therefore correspond to thermodynamic equilibrium of the two-component Zr–O mixture above the stability range of the low oxygen ordered phases, with Zr(O)_{sat}. We should note, however, that because phase formation and evolution at the oxide front in the present conditions are governed not only by thermodynamics but also by kinetics, the studies mentioned above provide only a rough guideline of what could be observed.

4.2. Oxide morphology

While the sequence of phases is similar in the three alloys, the layer thicknesses are quite different from one alloy to another. Crystal bar Zr exhibits the thinnest ZrO and Zr(O)_{sat} layers. Zircaloy-4 has distinct layers of ZrO and Zr(O)_{sat} of thicknesses of the order of 100 nm, while Zr-Fe-Cr shows a thicker ZrO layer (>200 nm) containing islands and plate-like structures of Zr(O)_{sat}. The thicknesses of the different sub-oxide layers in all alloys are compared in Table 4. In general, the lower the corrosion rate (derivative of the weight gain curve) at the point where the sample was collected, the thicker the suboxide layer, or alternatively, the more oxygen can diffuse ahead of the oxide. This is logical, as the oxide layers consume the suboxide as it advances, the faster the oxide growth, the less suboxide formation occurs [16]. In present study, the crystal bar Zr has fastest corrosion rate (see arrows in Fig. 1) and therefore thinnest ZrO and Zr(O)_{sat} layer. In contrast to the fastest growing oxide (crystal bar Zr) where the ZrO₂/ZrO, ZrO/Zr(O)_{sat} and Zr(O)_{sat}/Zr interfaces may be assumed to grow at the same rate, in the presence of alloying elements, the ZrO₂/ZrO and ZrO/Zr(O)_{sat} interfaces may be slowed down relative to the Zr(O)_{sat}/Zr interface, which would help explain the thicker Zr(O)_{sat} layers in Zircaloy-4 and possibly in Zr-Fe-Cr as well. However, it may be also possible that the thicker suboxide is a *cause* (rather than an effect) of the oxide advance slowdown. Further work is needed to elucidate this point.

The morphology of the layers is also of interest. In Zircaloy-4, while the ZrO₂/ZrO interface is flat, the interface between ZrO and Zr(O)_{sat} is uneven, showing broad semi-elliptical regions of ZrO advancing into a region of Zr(O)_{sat}. This difference in morphology may result from different nucleation and growth kinetics, possibly resulting from the Sn segregation observed in Zircaloy-4 in the “fingers” between ZrO grains which could constrain the growth of Zr(O)_{sat} front.

4.3. Alloying elements

4.3.1. Cr distribution

The solubility of Cr in Zr is very low leading to formation of second phase particles (C14 Zr(Fe,Cr)₂) with Fe [35]. Cr was occasionally observed in small clusters in the bulk metal and near the oxide interface in Zircaloy-4. Presence of such clusters (around 3.5 nm in size) was also reported by Hudson [23]. No such clusters were observed in the Zr-Fe-Cr alloy, but their presence cannot be excluded due to the limited sampling of atom probe tomography. Considering the inhomogeneous distribution of these Fe and Cr rich clusters, it is possible that the APT tips failed to capture them. No conclusion can be made so far on how Cr may affect the corrosion kinetics. In the present study, there is no indication of Cr segregation to grain boundaries in any of the three alloys, nor to dislocations in Zircaloy-4, even though the estimated diffusion distance

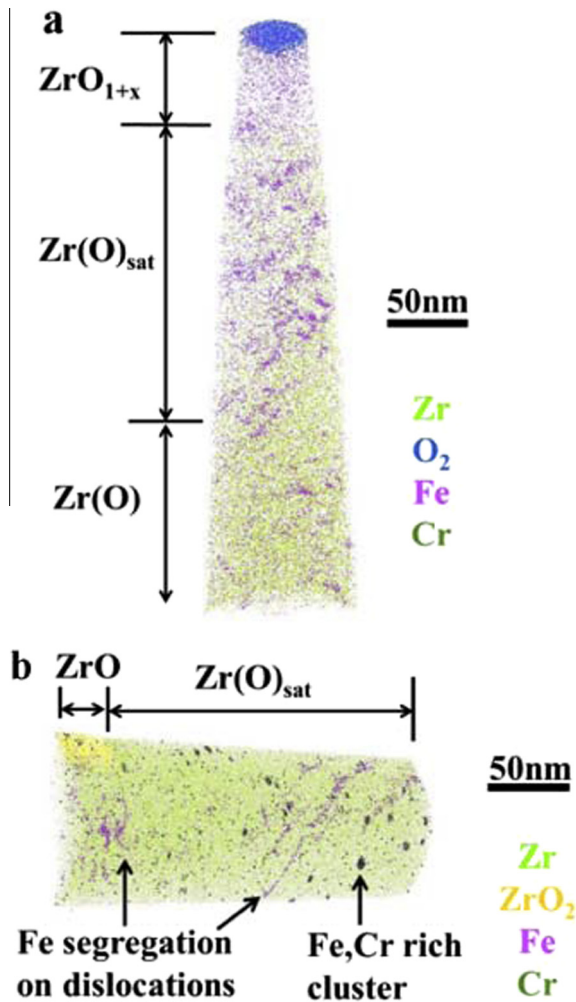


Fig. 11. Zircaloy-4 oxide region: (a) APT reconstruction showing segregation of Fe at dislocations in $Zr(O)_{sat}$ and solid solution; (b) APT reconstruction showing segregation of Fe at dislocations and Fe, Cr rich clusters in $Zr(O)_{sat}$.

for Cr at 360 °C is large based on the diffusion coefficient of Cr in Zr available in the literature [42,43]. The absence of Cr enrichment at grain boundaries also disagrees with the calculations by Christensen et al. [41]. A possible explanation would be that Cr is pinned at the second phases and clusters and therefore is not available to diffuse to grain boundaries.

4.3.2. Fe distribution

Similarly to Cr, Fe has very limited solubility in α -Zr leading to precipitation of second phase particles or segregation to dislocations and grain boundaries. As mentioned above APT observations of clusters is challenging due to the inhomogeneous distribution. It is also not clear if observed inhomogeneities in the oxide Fe distribution originate from previous inhomogeneities in the metal or if they originate in the oxide. Clusters were observed in Zircaloy-4, and expected in Zr–Fe–Cr but their presence in Zr–Fe–Cr remains to be confirmed. Yet, the presence of Fe clusters within the ZrO_2 phase in Zr–Fe–Cr, strongly suggests that there should be Fe clusters in Zr–Fe–Cr metal region that would have been incorporated into the advancing oxide front.

Segregation of Fe to grain boundaries is common to all three alloys both in the bulk region and near the oxide regions. Segregation of Fe on grain boundaries has also been reported by previous APT analyses in other Zr alloys [23,44,45]. When grain boundaries

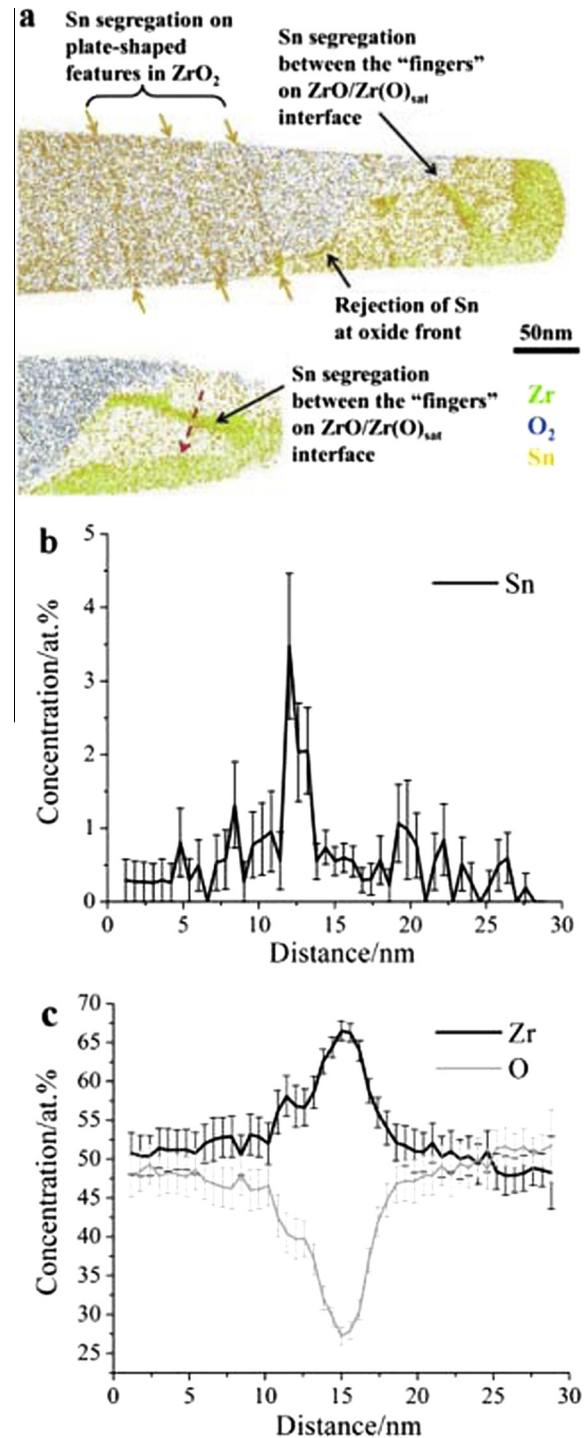


Fig. 12. Zircaloy-4 oxide region: (a) 10 nm slices taken from two distinct APT reconstructions showing distribution of Sn; (b) and (c) concentration profiles of Sn, Zr and O along the red arrow shown in (a).

extend from the metal to $Zr(O)_{sat}$, Fe segregation is also unchanged from the metal to the $Zr(O)_{sat}$ phase.

Fe also segregates to linear features, probably dislocations, which mostly run parallel to the $ZrO/Zr(O)_{sat}$ interface, as also found by Hudson [23]. Fe decorating dislocations is observed only in the $Zr(O)_{sat}$ layer and in the solid solution near the oxide/metal interface in Zircaloy-4 while it is absent in metal away from interface. The presence of dislocations can be rationalized in terms of local strains induced by the growing oxide. The lack of segregation of Fe to dislocations in the tip taken from crystal bar Zr is likely due to fewer dis-

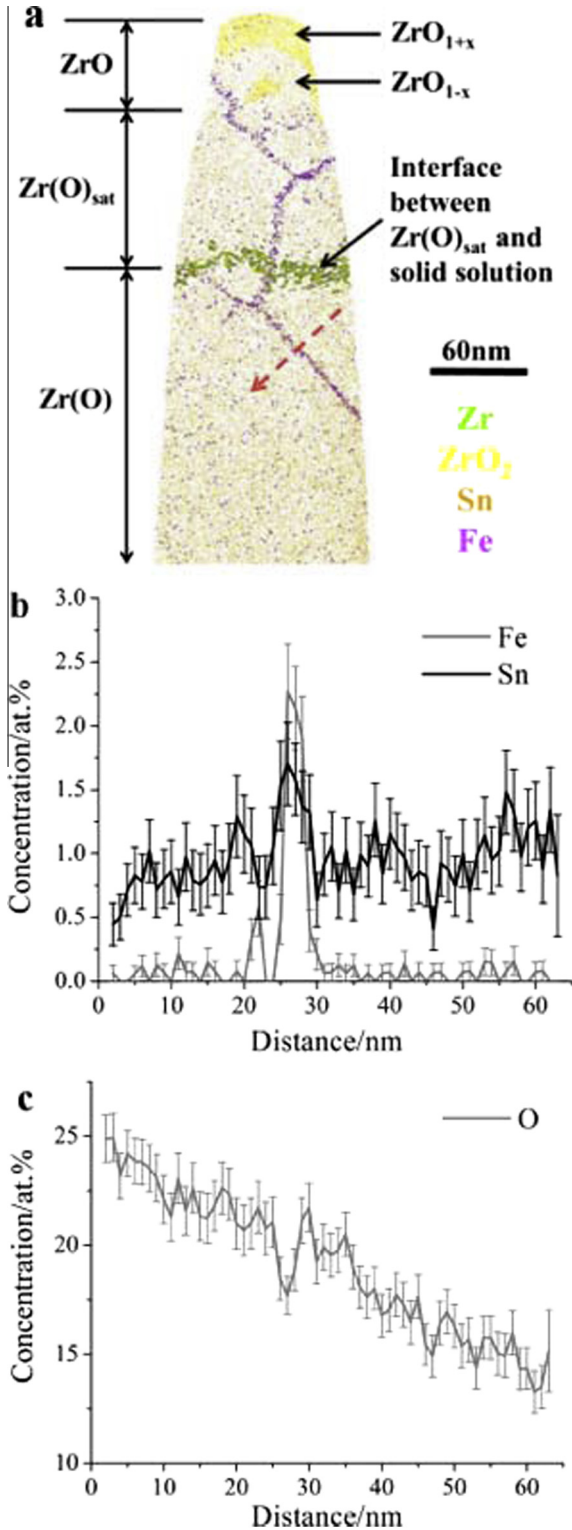


Fig. 13. Zircaloy-4 oxide region: (a) 10 nm slice from an APT reconstruction showing the segregation of Fe and Sn at the grain boundaries in the Zr(O)_{sat} and solid solution; (b) and (c) concentration profiles for Fe, Sn and O across the grain boundary along the red arrow shown in (a).

locations present near the interface, as the oxide is thin. It is also possible that the density of dislocations remarkably decreases in the presence of nearby grain boundaries, as captured in the reconstruction shown in Fig. 10(a). For the Zr–Fe–Cr alloy, most APT needles of Zr–Fe–Cr in this study fractured before reaching the Zr(O)_{sat} region;

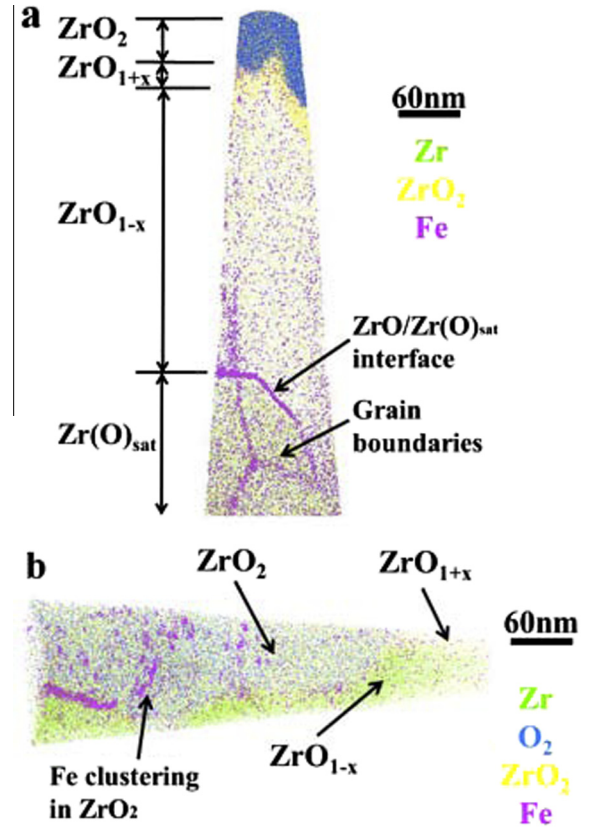


Fig. 14. Zr–Fe–Cr oxide region: (a) 10 nm slice one from APT reconstruction showing the Fe segregation at ZrO/Zr(O)_{sat} interface and at grain boundaries; (b) APT reconstruction showing the Fe clustering on planar and line features in ZrO₂.

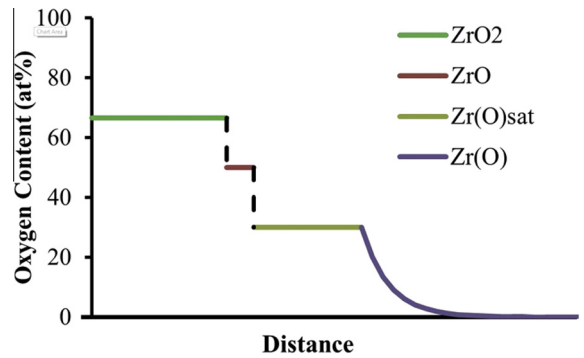


Fig. 15. Schematic sequence of phases ahead of the oxide front in Zr alloys.

and more work would be required to determine the Fe distribution beneath ZrO layer for this alloy.

The rejection of Fe ahead of ZrO₂ and ZrO fronts into Zr(O)_{sat} as the oxides advance is observed in crystal bar Zr (Fig. 10) and Zr–Fe–Cr (Fig. 11). The significantly different oxide growth rates in these two alloys challenges any role of Fe in changing the corrosion kinetics.

4.3.3. Sn distribution

Sn is a major alloying addition in Zircaloy-4 usually added to improve mechanical properties and creep resistance. Previous work on Zr–Sn–Nb alloys [26] suggested that Sn is incorporated into the oxide leading to a constant Sn/Zr ratio in both the oxide

Table 4

Approximate thickness of suboxide layers in all three alloys. The measured thickness only reflects the order of magnitude due to variation of layer thickness between different locations on the specimens.

Alloy	Suboxide phase	Approximate thickness (nm)
Crystal bar Zr	ZrO (ZrO _{1-x} and ZrO _{1+x})	Less than 20
	Zr(O) _{sat}	Less than 20
Zircaloy-4	ZrO (ZrO _{1-x} and ZrO _{1+x})	Around 50
	Zr(O) _{sat}	Around 100
Zr-Fe-Cr	ZrO (ZrO _{1-x} and ZrO _{1+x})	At least 200
	Zr(O) _{sat}	N.A. ^a

^a All APT specimens in present study fractured before reaching the Zr(O) so the thickness of Zr(O)_{sat} layer is not available.

and the metal. The present study however found that, the Sn/Zr ratio in ZrO₂ is a somewhat lower than that in the suboxides and the metal (see Table 3). This could be caused by rejection of Sn ahead of the oxide front. The rejection of Sn by the growth of ZrO₂ can also be demonstrated by the evidence of Sn being pinned on planar features (possibly grain boundaries) in ZrO₂ as well as segregation of Sn to ZrO₂/ZrO interface and ZrO/Zr(O)_{sat} interface. The segregation of Sn into what appears to be oxide grain boundaries could lend support to previously proposed ideas of changing oxide conductivity as a result of element segregation to oxide grain boundaries creating preferential paths for electron conduction [46].

5. Conclusions

A detailed study has been performed using atom probe tomography on oxide layers formed on three different Zr alloys (crystal bar Zr, Zircaloy-4 and Zr-0.4Fe-0.2Cr) when subjected to 360 °C water in an autoclave. Needles were obtained by focused ion beam and prepared either at the oxide metal interface or in the bulk of the material to discern the alloying elemental distribution with atomic scale resolution and fine concentration sensitivity. The results are as follows:

1. The alloying element distributions in the bulk of the alloys conform to what is previously known from TEM and other techniques, with the additional precision of the observation of Fe segregation to lattice defects such as grain boundaries and dislocations and the presence of Fe and Cr rich nano-precipitates.
2. The distribution of alloying elements is modified in the oxygen-rich region of the metal next to the oxide front. Segregation and clustering of Fe and Sn are observed along grain boundaries in ZrO₂, at ZrO₂/ZrO and ZrO/Zr(O)_{sat} interfaces.
3. A consistent sequence of sub-oxide phases is observed ahead of the ZrO₂ oxide front, consisting of (i) a thin layer of equiatomic ZrO (occasionally slightly over and under stoichiometric) (ii) saturated solid solution Zr(O)_{sat} with a constant oxygen concentration consistent with the Zr₂O stoichiometry, and (iii) a slowly decreasing oxygen profile into the metal.
4. The morphology of the interfaces varies between different oxide phases, being flat between ZrO₂ and ZrO and rugged between ZrO and Zr(O)_{sat}.

Acknowledgments

This research was supported by the DOE Office of Nuclear Energy's Nuclear Energy University Program and the University of Michigan College of Engineering.

References

- [1] C. Lemaignan, A.T. Motta, Zirconium alloys in nuclear applications, in: B.R.T. Frost (Ed.), *Materials Science and Technology, A Comprehensive Treatment*, vol. 10B, VCH, New York, 1994, pp. 1–51.
- [2] A.T. Motta, *Journal of Metals* 63 (2011) 59–63.
- [3] G.P. Sabol, ZIRLO an alloy development success, in: 14th ASTM International Symposium on Zr in the Nuclear Industry, Stockholm, STP1467, 2005, pp. 3–24.
- [4] G.L. Garner, J.P. Mardon, *Nuclear Engineering International* (2002) 36.
- [5] Hillner, Corrosion of zirconium-base alloys – an overview, in: 3rd International Symposium on Zr in the Nuclear Industry, ASTM, STP 633, 1977, pp. 211–235.
- [6] T. Ahmed, L.H. Keys, *Journal of the Less-Common Metals* 39 (1975) 99–107.
- [7] B. Cox, *Journal of Nuclear Materials* 28 (1968) 1–47.
- [8] B. Cox, *Journal of Nuclear Materials* 336 (2005) 331–368.
- [9] D. Pecheur, *Journal of Nuclear Materials* 278 (2000) 195–201.
- [10] D. Pecheur, F. Lefebvre, A.T. Motta, C. Lemaignan, D. Charquet, Oxidation of intermetallic precipitates in Zircaloy-4: IMPACT of irradiation, in: 10th International Symposium on Zirconium in the Nuclear Industry, Baltimore, MD, ASTM STP 1245, 1994, pp. 687–705.
- [11] D. Pecheur, F. Lefebvre, A.T. Motta, C. Lemaignan, J.-F. Wadier, *Journal of Nuclear Materials* 189 (1992) 2318–2332.
- [12] J.P. Pemsler, *Electrochemical Technology* 4 (1966) 128–131.
- [13] J. Godlewski, How the tetragonal zirconia is stabilized in the oxide scale that is formed on a zirconium alloy corroded at 400 °C in steam, in: 10th International Symposium on Zr in the Nuclear Industry, ASTM STP 1245, 1994, pp. 663–686.
- [14] A.T. Motta, M.J. Gomes da Silva, A. Yilmazbayhan, R.J. Comstock, Z. Cai, B. Lai, *Journal of ASTM International* 5 (2008). paper ID# JAI10125.
- [15] A. Yilmazbayhan, E. Breval, A. Motta, R. Comstock, *Journal of Nuclear Materials* 349 (2006) 265–281.
- [16] A. Yilmazbayhan, A.T. Motta, R.J. Comstock, G.P. Sabol, B. Lai, Z. Cai, *Journal of Nuclear Materials* 324 (2004) 6–22.
- [17] P. Bossis, G. Lelievre, P. Barberis, X. Iltis, F. Lefebvre, Multi-scale characterization of the metal-oxide interface of zirconium alloys, in: Zirconium in the Nuclear Industry: Twelfth international Symposium, West Conshohocken, PA, ASTM STP 1354, 2000, pp. 918–945.
- [18] B. Hutchinson, B. Lehtinen, M. Limbach, M. Dahlback, A Study of the structure and chemistry in Zircaloy-2 and the resulting oxide after high temperature corrosion, in: Zirconium in the Nuclear Industry: Fifteenth international Symposium, Sunriver, OR, United States, American Society for Testing and Materials ASTM STP 1505, 2009, pp. 269–284.
- [19] N. Ni, D. Hudson, J. Wei, P. Wang, S. Lozano-Perez, G.D.W. Smith, J.M. Sykes, S.S. Yardley, K.L. Moore, S. Lyon, R. Cottis, M. Preuss, C.R.M. Grovenor, *Acta Materialia* 60 (2012) 7132–7149.
- [20] N. Ni, S. Lozano-Perez, J. Sykes, C. Grovenor, *Ultramicroscopy* 111 (2011) 123–130.
- [21] B. Wadman, H.-O. Andren, microanalysis of the matrix and the oxide-metal interface of uniformly corroded Zircaloy, in: Zirconium in the Nuclear Industry: Ninth international Symposium, Kobe, Japan, ASTM STP 1132, 1991, pp. 461–475.
- [22] M. Thuvander, H.-O. Andren, *Ultramicroscopy* 111 (2011) 711–714.
- [23] D. Hudson, Zirconium Oxidation on the Atomic Scale, PhD thesis, Department of Materials, University of Oxford, 2010.
- [24] G. Sundell, M. Thuvander, H.-O. Andren, *Corrosion Science* 65 (2012) 10–12.
- [25] P. Tejlund, M. Thuvander, H.-O. Andren, S. Ciurea, T. Andersson, M. Dahlback, L. Hallstadius, *Journal of ASTM International* 8 (2011). paper ID# JAI102956.
- [26] J. Wei, P. Frankel, E. Polatidis, M. Blat, A. Ambar, R.J. Comstock, L. Hallstadius, D. Hudson, G.D.W. Smith, C.R.M. Grovenor, M. Klaus, R.A. Cottis, S. Lyon, M. Preuss, *Acta Materialia* 61 (2013) 4200–4214.
- [27] A. Motta, A. Yilmazbayhan, M. Gomes da Silva, R.J. Comstock, G. Was, J. Busby, E. Gartner, Q. Peng, Y.H. Jeong, J.Y. Park, *Journal of Nuclear Materials* 371 (2007) 61–75.
- [28] X. Iltis, F. Lefebvre, C. Lemaignan, Microstructure evolution and iron redistribution in Zircaloy oxide layers: comparative effects of neutron irradiation flux and irradiation damages, in: 11th International Symposium on Zirconium in the Nuclear Industry, Garmisch-Partenkirchen, ASTM STP 1295 1996, pp. 242–264.
- [29] Q. Peng, E. Gartner, J.T. Busby, A.T. Motta, G.S. Was, *Corrosion* 63 (2007) 577–590.
- [30] M. Preuss, P. Frankel, S. Lozano-Perez, D. Hudson, E. Polatidis, N. Ni, J. Wei, C. English, S. Storer, K.B. Chong, M. Fitzpatrick, P. Wang, J. Smith, C. Grovenor, G. Smith, J. Sykes, B. Cottis, S. Lyon, L. Hallstadius, R.J. Comstock, A. Ambar, M. Blat-Yrieix, *Journal of ASTM International* 8 (2011). paper ID#JAI103246.
- [31] A. Yilmazbayhan, O. Delaire, A.T. Motta, R.C. Birtcher, J.M. Maser, B. Lai, *Journal of Nuclear Materials* 21 (2003) 221–232.
- [32] K. Thompson, D. Lawrence, D.J. Larson, J.D. Olson, T.F. Kelly, B. Gorman, *Ultramicroscopy* 107 (2007) 131–139.
- [33] T.T. Tsong, *Surface Science* 70 (1978) 211–233.
- [34] H. Zou, G.M. Hood, J.A. Roy, R.J. Schultz, J.A. Jackman, *Journal of Nuclear Materials* 210 (1994) 239–243.
- [35] D. Charquet, R. Hahn, E. Ortlieb, J.-P. Gros, J.-F. Wadier, Solubility limits and formation of intermetallic precipitates in ZrSnFeCr alloys, in: Zirconium in the Nuclear Industry: 8th International Symposium, ASTM, STP 1023, 1989, pp. 405–422.

- [36] D. Charquet, E. Alheritiere, Second phase particles and matrix properties on Zircalloys, in: Workshop on Second-Phase particles in Zircaloy, Erlangen, Germany, F.R.G. Kerntechnische Gesellschaft 1985, pp. 5–11.
- [37] A. Morley, G. Sha, S. Hirose, A. Cerezo, G.D.W. Smith, *Ultramicroscopy* 109 (2009) 535–540.
- [38] J.P. Abriata, J. Garces, R. Versaci, *Bulletin of Alloy Phase Diagrams* 7 (1986) 116.
- [39] R. Arroyave, L. Kaufman, T.W. Eagar, *Calphad* 26 (2002) 95–118.
- [40] B. Puchaka, A. Van der Ven, *Physical Review B* (2013) (accepted for publication).
- [41] M. Christensen, T.M. Angerliu, J.D. Balard, J. Vollmer, R. Najafabadi, E. Wimmer, *Journal of Nuclear Materials* 404 (2010) 121–127.
- [42] G.M. Hood, *Journal of Nuclear Materials* 159 (1988) 149–175.
- [43] B.M. Pande, M.C. Naik, R.P. Agarwala, *Journal of Nuclear Materials* 28 (1968) 324–332.
- [44] D. Hudson, G.D.W. Smith, *Scripta Materialia* 61 (2009) 411–414.
- [45] B. Gault, P.J. Felfel, M. Ivermark, H. Bergqvist, J.M. Cairney, S.P. Ringer, *Materials Letters* 91 (2013) 63–66.
- [46] K. Takeda, H. Anada, Mechanism of corrosion degradation in Sn, in: 12th International Symposium on Zr in the Nuclear Industry, ASTM STP 1354, 2000, pp. 592–608.